Controlled nitric oxide production via $O(^1D)+N_2O$ reactions for use in oxidation flow reactor studies

Andrew Lambe[1,2], Paola Massoli[1], Xuan Zhang[1], Manjula Canagaratna[1], John Nowak[1,*], Chao Yan[3], Wei Nie[4,3], Timothy Onasch[1,2], John Jayne[1], Charles Kolb[1], Paul Davidovits[2], Douglas Worsnop[1,3], and William Brune[5]

[1]Aerodyne Research, Inc., Billerica, Massachusetts, United States
[2]Chemistry Department, Boston College, Chestnut Hill, Massachusetts, United States
[3]Physics Department, University of Helsinki, Helsinki, Finland
[4]Joint International Research Laboratory of Atmospheric and Earth System Sciences, School of Atmospheric Sciences, Nanjing University, Nanjing, China
[5]Department of Meteorology and Atmospheric Sciences, The Pennsylvania State University, University Park, Pennsylvania, United States
[*]Current address: Chemistry and Dynamics Branch, NASA Langley Research Center, Hampton, Virgina, United States

Correspondence to: Andrew Lambe (lambe@aerodyne.com), William Brune (whb2@psu.edu)

Abstract.

Oxidation flow reactors that use low-pressure mercury lamps to produce hydroxyl (OH) radicals are an emerging technique for studying the oxidative aging of organic aerosols. Here, ozone (O_3) is photolyzed at 254 nm to produce $O(^1D)$ radicals, which react with water vapor to produce OH. However, the need to use parts-per-million levels of O_3 hinders the ability of oxidation flow reactors to simulate NO_x-dependent SOA formation pathways. Simple addition of nitric oxide (NO) results in fast conversion of NO_x (NO + NO_2) to nitric acid (HNO_3), making it impossible to sustain NO_x at levels that are sufficient to compete with hydroperoxy (HO_2) radicals as a sink for organic peroxy (RO_2) radicals. We developed a new method that is well suited to the characterization of NO_x-dependent SOA formation pathways in oxidation flow reactors. NO and NO_2 are produced via the reaction $O(^1D) + N_2O \rightarrow 2NO$, followed by the reaction $NO + O_3 \rightarrow NO_2 + O_2$. Laboratory measurements coupled with photochemical model simulations suggest that $O(^1D) + N_2O$ reactions can be used to systematically vary the relative branching ratio of RO_2 + NO reactions relative to RO_2 + HO_2 and/or RO_2 + RO_2 reactions over a range of conditions relevant to atmospheric SOA formation. We demonstrate proof of concept using high-resolution time-of-flight chemical ionization mass spectrometer (HR-ToF-CIMS) measurements with nitrate (NO_3^-) reagent ion to detect gas-phase oxidation products of isoprene and α-pinene previously observed in NO_x-influenced environments and in laboratory chamber experiments.

1 Introduction

Recent atmospheric observations supported by experimental and theoretical studies show that highly oxygenated, extremely low-volatility organic compounds (ELVOC), together with sulfuric acid, are involved in the initial nucleation steps leading to new particle formation (NPF) (Donahue et al., 2013; Riccobono et al., 2014). ELVOC form rapidly in the gas phase via

auto-oxidation processes (Crounse et al., 2013; Rissanen et al., 2014) and tend to condense irreversibly (Ehn et al., 2014). Following NPF, semivolatile organic compounds (SVOC) with higher vapor pressures condense on newly formed aerosols at rates influenced by their volatility (Donahue et al., 2012), ultimately driving nanoparticle growth towards formation of cloud condensation nuclei (CCN) (Pierce et al., 2012; Riipinen et al., 2012). NPF events may produce as much as 50% of global CCN (Merikanto et al., 2009; Yu and Luo, 2009). However, mechanisms that govern the formation of specific ELVOCs and condensation of SVOCs in various source regions are largely unknown.

The extent to which NPF and growth is influenced by natural and anthropogenic emissions separately and together, is still unknown. In some locations, biogenic SOA formation is enhanced by anthropogenic carbonaceous aerosol particles, SO_x and/or NO_x (Carlton et al., 2010; Shilling et al., 2013; Xu et al., 2015). At the moment, one can only speculate about some of the possible synergistic or antagonistic chemical mechanisms regulating these processes. For example, anthropogenic emissions can enhance biogenic SOA formation by providing seed particles for condensable biogenic vapors. On the other hand, isoprene can slow down the formation of SOA from other volatile organics, possibly by depleting the local concentration of OH without itself producing significant SOA yields (Pugh et al., 2011). Globally the source strength of anthropogenic SOA is poorly constrained, with an uncertainty of at least a factor of 2 or 3 (Spracklen et al., 2011). Large uncertainties in pre-industrial aerosol emissions and processes further confound our understanding of the direct and indirect effects of anthropogenic aerosol emissions (Carslaw et al., 2014) and the impact of aerosols on climate (Andreae and Gelencsér, 2006).

To date, environmental chamber experiments have generated most of the laboratory SOA yield data used in atmospheric models, especially in simulations of polluted atmospheric conditions with elevated NO_x concentrations. However, NO_x-dependent chambers studies are complicated by the need to use multiple OH radical precursors such as hydrogen peroxide (H_2O_2) and nitrous acid (HONO) or methyl nitrite (CH_3ONO) to span the relevant range of NO_x levels (typically, H_2O_2 for low-NO_x conditions and HONO or CH_3ONO for high-NO_x conditions) (Ng et al., 2007). Additionally, chambers have relatively low throughput and are limited to residence times of several hours due to chamber deflation and/or loss of particles and oxidized vapors to the chamber walls (Zhang et al., 2014). This restricts environmental chambers to simulating atmospheric aerosol particle lifetimes and SOA yields only up to 1 or 2 days, therefore limiting the study of formation of highly oxygenated SOA characteristic of aged atmospheric organic aerosol PM (Ng et al., 2010) unless very low VOC precursor concentrations are used (Shilling et al., 2009; Pfaffenberger et al., 2013).

Oxidation flow reactors have recently been developed to study SOA formation and evolution over time scales ranging from hours to multiple days of equivalent atmospheric OH exposure. In these reactors, O_3 is photolyzed at 254 nm to produce $O(^1D)$ radicals, which react with water vapor to produce OH radicals. OH concentrations are typically 10^8 cm^{-3} or greater. Under these conditions, atmospheric photochemical aging timescales up to ∼10 days can be simulated at flow tube residence times of a few minutes or less. Recent experimental studies suggest that flow reactor-generated SOA particles have compositions similar to SOA generated in smog chambers (Bruns et al., 2015; Lambe et al., 2015) and in the atmosphere (Tkacik et al., 2014; Ortega et al., 2016; Palm et al., 2016). Modeling studies suggest that flow reactors can simulate tropospheric oxidation reactions with minimal experimental artifacts (Li et al., 2015; Peng et al., 2015, 2016). A limitation of flow reactors is the need to use parts-per-million levels of O_3, hindering the possibility to efficiently simulate NO_x-dependent SOA formation pathways. Simple

addition of NO to flow reactors, while possible (Liu et al., 2015), cannot sustain NO_x mixing ratios at levels that are sufficient to compete with hydroperoxy (HO_2) radicals as a sink for organic peroxy (RO_2) radicals due to fast conversion of NO_x to nitric acid (HNO_3). Here, we present a new method well suited to the characterization of NO_x-dependent SOA formation pathways in oxidation flow reactors. We validate the concept using high-resolution time-of-flight chemical ionization mass spectrometer measurements (HR-ToF-CIMS) to detect gas-phase oxidation products of isoprene and α-pinene that have been observed in NO_x-influenced environments and laboratory chamber experiments.

2 Experimental

Experiments were conducted using an Aerodyne Potential Aerosol Mass (PAM) oxidation flow reactor, which is a horizontal 13.3 L aluminum cylindrical chamber (46 cm long $\times$ 22 cm ID) operated in continuous flow mode (Kang et al., 2007; Lambe et al., 2011a). The average residence time was 80 s. The relative humidity (RH) in the reactor was controlled in the range of 3–35 % at 22°C, corresponding to H_2O mixing ratios of approximately 0.07 - 1%. The irradiance in the reactor was measured using a photodiode (TOCON-C6, sglux Gmbh). The gas-phase SOA precursors used in these studies include two biogenic compounds (isoprene, α-pinene) that were prepared in compressed gas cylinders and introduced to the reactor at controlled rates using a mass-flow controller. Mixing ratios of the gas-phase precursors entering the reactor were 36 ppb for isoprene (diluted from 1000 ppm in N_2, Matheson) and 15 ppb for α-pinene (diluted from 150 ppm in N_2, Matheson). These mixing ratios are a factor of 3 to 10 lower than mixing ratios that are typically required to induce homogenous nucleation of condensible oxidation products in related oxidation flow reactor studies (Lambe et al., 2011b).

2.1 OH radical and NO_x generation

OH radicals were produced in the reactor via the reaction $O(^1D) + H_2O \rightarrow 2OH$, with $O(^1D)$ radicals produced from the reaction $O_3 + h\nu \rightarrow O_3 + O(^1D)$. O_3 ($\sim$5 ppm) was generated outside the flow reactor by O_2 irradiation at 185 nm using a mercury fluorescent lamp (GPH212T5VH, Light Sources, Inc.). $O(^1D)$ was produced by photolysis of O_3 at 254 nm inside the reactor using two mercury fluorescent lamps (GPH436T5L, Light Sources, Inc). A fluorescent dimming ballast was used to regulate current applied to the lamps. To vary [OH] inside the reactor, I_{254} was varied by changing the dimming voltage applied to the ballast between 1.6 and 10 VDC. At these conditions, I_{254} ranged from approximately $(0.064 - 3.2) \times 10^{15}$ ph cm^{-2} sec. The highest I_{254} value was calculated from the internal surface area of the reactor and the lamp output at maximum intensity (e.g. 10 VDC) specified by the manufacturer. Lower I_{254} values were calculated from the measured irradiance at lower dimming voltage relative to the measured irradiance and manufacturer-specified lamp output at 10 VDC.

NO and NO_2 were produced via the reaction $N_2O + O(^1D) \rightarrow 2NO$, followed by the reaction $NO + O_3 \rightarrow NO_2$. N_2O (99.5%) was introduced from a compressed gas cylinder at flow rates ranging from 0 to 648 cm^3 min^{-1}, corresponding to mixing ratios of 0% to 5.6% at the carrier gas flow rates that were used. Using N_2O as the NO_x precursor has the following advantages over the simple addition of NO to the carrier gas. First, due to continuous production of $O(^1D)$ from O_3 photolysis inside the reactor (along with minor consumption of N_2O), the spatial distribution of NO and NO_2 is more homogenous.

Second, attainable steady-state mixing ratios of NO from $N_2O + O(^1D)$ reactions (ppb levels) are orders of magnitude higher than simple NO injection (sub-ppt levels) as inferred from photochemical model simulations described below in Sect. 2.3. Third, photolysis of N_2O at 185 nm (if used) provides an additional source of $O(^1D)$ from the reaction $N_2O + h\nu \rightarrow N_2 + O(^1D)$. We assume background [NO] < 0.05 ppb in the reactor based on separate [NO] measurements and calculate additional NO
5   formed from $N_2O + O(^1D)$ reactions using the model described in Sect. 2.3.

NO$_3$ radicals, which are produced as a byproduct of $NO_2 + O_3$ or $HNO_3 + OH$ reactions, can potentially convolute interpretation of results if the relative oxidation rates of isoprene/α-pinene by OH and NO$_3$ are comparable. For results presented in Sects. 3.2 and 3.3, calculated OH, O$_3$ and NO$_3$ exposures combined with published OH, O$_3$ and NO$_3$ rate constants (Atkinson, 1986, 1991) suggest that the relative contribution of NO$_3$ to isoprene and α-pinene oxidation ranges from approximately
10   0 to 4% and 0 to 40%, respectively, as a function of [N$_2$O]. Thus, reaction rates of α-pinene with OH, O$_3$ and NO$_3$ may be comparable under a subset of experimental conditions. Potential implications are discussed in more detail in Sect. 3.3.

2.2   Chemical ionization mass spectrometer (CIMS) measurements

Mass spectra of isoprene and α-pinene gas-phase oxidation products were obtained with an Aerodyne high-resolution time-of-flight mass spectrometer (Bertram et al., 2011) coupled to an atmospheric pressure interface with a nitrate ion chemical ioniza-
15   tion source (NO$_3^-$-HRToF-CIMS, hereafter abbreviated as "NO$_3^-$-CIMS") (Eisele and Tanner, 1993; Ehn et al., 2012). Nitrate (NO$_3^-$) and its higher order clusters (e.g. HNO$_3$NO$_3$) generated from x-ray ionization of HNO$_3$ were used as the reagent due to the selectivity to highly oxidized organic compounds, including species that contribute to SOA formation (Ehn et al., 2014; Krechmer et al., 2015). Isoprene and α-pinene oxidation products were detected as adducts with NO$_3^-$ or HNO$_3$NO$_3^-$. CIMS data were analyzed using the Tofware software package (Tofwerk AG, Aerodyne Research, Inc.) implemented in IGOR Pro 6
20   (Wavemetrics, Inc.). The output of the PAM oxidation flow reactor was sampled at 10.5 $Lmin^{-1}$ through a 2' length of 0.75" OD stainless steel tubing inserted directly into the rear feedthrough plate of the reactor.

2.3   Photochemical modeling

We used a photochemical model Li et al. (2015); Peng et al. (2015) implemented in MATLAB (Mathworks) to calculate concentrations of radical/oxidant species produced in the reactor. Model input parameters included pressure, temperature, [H$_2$O],
25   [O$_3$], [N$_2$O], I_{254}, mean residence time, and the input mixing ratios of isoprene and α-pinene. Differential equations used to describe the radical/oxidant chemistry were integrated at 5 millisecond time steps. The following reactions and associated kinetic rate constants (Sander et al., 2000, 2006) were implemented to describe NO$_x$ chemistry in the reactor:

$$N_2O + h\nu \rightarrow N_2 + O(^1D) \tag{R1}$$

$$N_2O + O(^1D) \rightarrow 2NO \tag{R2}$$

$$N_2O + O(^1D) \rightarrow N_2 + O_2 \tag{R3}$$

$$NO + OH \rightarrow HONO \tag{R4}$$

$$NO + HO_2 \rightarrow OH + NO_2 \tag{R5}$$

$$NO + O_3 \rightarrow NO_2 + O_2 \tag{R6}$$

$$NO_2 + O \rightarrow NO + O_2 \tag{R7}$$

$$NO_2 + O_3 \rightarrow NO_3 + O_2 \tag{R8}$$

$$NO_3 + O \rightarrow NO_2 + O_2 \tag{R9}$$

$$HONO + OH \rightarrow H_2O + NO_2 \tag{R10}$$

$$NO_2 + NO_3 + M \rightleftharpoons N_2O_5 + M \tag{R11}$$

$$NO + NO_3 \rightarrow 2NO_2 + O_2 \tag{R12}$$

$$NO_2 + OH + M \rightarrow HNO_3 + M \tag{R13}$$

$$NO_2 + HO_2 + M \rightarrow HNO_4 + M \tag{R14}$$

$$N_2O_5 + H_2O \rightarrow 2HNO_3 \tag{R15}$$

$$HNO_4 + OH \rightarrow products \tag{R16}$$

$$HNO_3 + OH \rightarrow H_2O + NO_3 \tag{R17}$$

$$NO_3 + NO_3 \rightarrow 2NO_2 + O_2 \tag{R18}$$

Calculated OH exposures (product of mean OH concentration and residence time) ranged from 1.7×10^{10} to 2.1×10^{12} molec cm^{-3} sec or approximately 3 hours to 16 days of equivalent atmospheric exposure at [OH] = 1.5×10^6 cm^{-3} (Mao et al., 2009). Steady-state [NO] and [HO$_2$] ranged from 0 to 13.5 ppb and 0.01 to 2.1 ppb, respectively, depending on [N$_2$O], [H$_2$O], [O$_3$] and I$_{254}$. We assumed $\pm 25\%$ uncertainty in the calculated OH exposure and $\pm 60\%$ uncertainty in other model outputs (Peng et al., 2015). For ratios of model outputs with independent $\pm 60\%$ uncertainties (e.g. NO:HO$_2$), propagated uncertainties of $\pm 85\%$ were assumed. Addition of N$_2$O at the highest mixing ratios that were used suppressed [OH] because N$_2$O competes with H$_2$O as a sink for O(^{1}D). Potential consequences of OH suppression are discussed where applicable in Sects. 3.2 and 3.3.

3 Results and Discussion

3.1 Optimal reactor operating conditions for $O(^1D) + N_2O +$ reactions

To investigate optimal operating conditions for NO_x generation, we implemented the model described in Sect. 2.3 over I_{254}, $[O_3]$, and $[H_2O]$ values ranging from 3.2×10^{13} to 6.4×10^{15} ph cm^{-2} sec^{-1}, 0.5 to 50 ppm, and 0.07 to 2.3% at 22°C,

5 respectively, as a function of $[N_2O]$ = 0 to 5%. These values span the nominal range of operating conditions that can be achieved with the PAM reactor. To facilitate independent evaluation of the effects of $[O_3]$ and I_{254} on $[NO]$, we restricted our analysis to conditions that use only 254 nm photolysis. Using both 185 and 254 nm photolysis provides additional sources of $O(^1D)$ and OH from N_2O and H_2O photolysis at 185 nm, respectively, at the expense of independent control of $[O_3]$ and I_{254}.

Figure 1 shows the modeled steady-state $[NO]$ in the reactor as a function of $[N_2O]$ = 0 to 5%, assuming a mean residence

10 time of 80 sec, $[H_2O]$ = 1%, and $[O_3]$ = 5 ppm. In addition, Figs. S1 - S3 in the Supplement show modeled $NO:HO_2$ and $OH:NO_3$ ratios as a function of input $[N_2O]$, with I_{254}, $[O_3]$, and $[H_2O]$ each varied individually while other input conditions are fixed. The following observations that are evident from Figs. 1 and S1 - S3 were used to constrain the optimal oxidant conditions. First, at fixed $[O_3]$, $[H_2O]$, and $[N_2O]$, increasing I_{254} increases $[O(^1D)]$ and consequently $[NO]$. Second, at fixed I_{254}, $[H_2O]$, and $[N_2O]$, decreasing $[O_3]$ increases $[OH]:[NO_3]$ by decreasing NO_2 formation from $NO + O_3$ reactions, and

15 consequently NO_3 formation from $NO_2 + O_3$ reactions. At lower $[N_2O]$, increasing $[O_3]$ increases $[NO]$ because greater NO production from higher $[O(^1D)]$ offsets greater NO loss from reaction with O_3. On the other hand, at higher $[N_2O]$, greater O_3 loss from reaction with NO_2 offsets greater NO production from higher $[N_2O]$. Third, at fixed I_{254}, $[O_3]$, and $[N_2O]$, increasing $[H_2O]$ increases $[OH]:[NO_3]$ by increasing OH production from $H_2O + O(^1D)$ reactions. The relative importance of these operating conditions is situationally dependent on the relative OH, O_3, and NO_3 rate constants of the target species

20 and photochemical age. To demonstrate proof of principle, we present NO_3^--CIMS spectra of isoprene and α-pinene oxidation products in the following sections.

3.2 NO_3^--CIMS spectra of isoprene oxidation products

Figure 2 shows NO_3^--CIMS mass spectra of products generated from the oxidation of isoprene (C_5H_8) that cluster with NO_3^- ions to form NO_3^--species adducts. Ion signals are plotted as a function of mass-to-charge ratio (m/Q). NO_3 adduct formation

25 is a relatively low-energy process that does not result in fragmentation of the analyte (Eisele and Tanner, 1993; Kurtén et al., 2011). Thus, the measured ion signals are directly related to the chemical formula of individual species that are generated in the reactor. Ion signals corresponding to isoprene oxidation products shown in Fig. 2 were colored based on classification in ion groups containing 4-5 carbon atoms with zero ($C_{4-5}H_{4-12}O_{3-8}$), one ($C_5H_{7-11}O_{3-8}NO_3$), and two ($C_5H_{10}O_{2-4}(NO_3)_2$) nitrogen atoms, where we assumed that nitrogen atoms were associated with nitrate functional groups and not heterocyclic

30 compounds. We also assume that nitrate functional groups are formed from $RO_2 + NO$ reactions (Sect. 2.1).

To generate spectra shown in Fig. 2, the reactor was operated at I_{254} = 6.4×10^{13} and 3.2×10^{15} ph cm^{-2} sec^{-1}, $[H_2O]$ = 1%, and $[N_2O]$ = 0 and 3%. As shown in Figs. S4 and S5, corresponding OH exposures ranged from $(1.7 - 2.0) \times 10^{10}$ (Fig. 2a and b) and $(0.52 - 2.1) \times 10^{12}$ molec cm^{-3} sec (Fig. 2c and d), respectively. At low OH exposure, the OH suppression at "high

NO$_x$" relative to "low NO$_x$" was comparatively minor (15%), whereas at high OH exposure, the OH suppression at "high NO$_x$" relative to 'low NO$_x$' was larger (75%). At the "high-NO$_x$" OH exposure of 5.2×10^{11} molec cm^{-3} sec, isoprene can react with OH up to 52 times in the reactor. This presumably exceeds the number of OH reactions (followed by RO$_2$ + NO reactions) that are necessary to fragment or condense oxidation products to the point where they are no longer detected with

5   NO$_3^-$-CIMS. Thus, it is unlikely that OH suppression at "high OH" and "high NO$_x$" significantly affected the NO$_3^-$-CIMS spectra shown in Fig. 2.

3.2.1   NO$_3^-$-CIMS spectral features observed at "low NO$_x$" conditions

C$_{4-5}$H$_{4-12}$O$_{3-8}$ ions comprised 93% and 97% of the signals at low and high OH exposure, respectively (inset pie charts in Figs. 2a and Fig. 2c). The C$_5$H$_{7-11}$O$_{3-8}$NO$_3$ signals that were observed here may be due to background NO$_x$ in the reactor

10   (Sect. 2.1). The signal at m/Q = 230, C$_5$H$_{12}$O$_6$ (NO$_3^-$ omitted for brevity here and elsewhere), was the largest signal detected at both low and high OH exposures at "low-NO$_x$" conditions. This species is likely a second-generation oxidation product that contains two hydroxyl (OH) and two peroxide (OOH) functional groups (Krechmer et al., 2015; St Clair et al., 2016) and is typically associated with isoprene SOA formation and growth under "low-NO$_x$" conditions. (Liu et al., 2016) Signals in Figs. 2c-d are approximately 10 times higher than in Figs. 2a-b because additional OH exposure produces higher yields of

15   multi-generation oxidation products that are detected with NO$_3^-$-CIMS.

Previously-identified multi-generation isoprene oxidation products such as C$_5$H$_{10}$O$_5$, C$_5$H$_{12}$O$_5$, and C$_5$H$_{10}$O$_6$ (Surratt et al., 2006; Krechmer et al., 2015; St Clair et al., 2016) were also detected at significant intensity under low-NO$_x$ conditions. When the OH exposure was increased by a factor of 100 from 2.0×10^{10} to 2.1×10^{12} molec cm^{-3} sec, the signal at C$_5$H$_{12}$O$_6$ increased by a factor of 10 and the signal at m/Q = 246, C$_5$H$_{12}$O$_7$, increased by a factor of 5. At high OH exposure, C$_5$H$_{12}$O$_7$

20   was the second-largest peak in the spectrum. These highly oxygenated isoprene oxidation products are likely also important in SOA formation processes. We note that C$_5$H$_{10}$O$_7$ is a proposed third-generation, tri-hydroperoxy carbonyl product of isoprene + OH in the absence of NO$_x$ (Peeters et al., 2014).

We hypothesize two reasons for the prominence of C$_5$H$_{10}$O$_7$, C$_5$H$_{12}$O$_7$, and C$_5$H$_{10}$O$_8$ in our spectra. First, NO$_3^-$ is more selective to highly oxidized species than other reagent ions (Surratt et al., 2006; Liu et al., 2016). Second, higher OH exposures

25   were achieved in the reactor than in environmental chambers. For example, the spectra shown in Figs. 2a and 2b were obtained at integrated OH exposures of 1.7×10^{10} and 2.1×10^{12} molec cm^{-3} sec, respectively, compared to an OH exposure of 8.6×10^9 molec cm^{-3} sec in the environmental chamber NO$_3^-$-CIMS measurements conducted by Krechmer et al. (2015).

3.2.2   NO$_3^-$-CIMS spectral features observed at "high NO$_x$" conditions

Following addition of N$_2$O at ~3% mixing ratio, the NO$_3^-$-CIMS spectra changed significantly at low and high OH exposures

30   (Figs. 2b and d). The signals of C$_{4-5}$H$_{4-12}$O$_{3-8}$ oxidation products decreased, and the signals of C$_5$H$_{7-11}$O$_{3-8}$NO$_3$ and C$_5$H$_{10}$O$_{2-4}$(NO$_3$)$_2$ oxidation products increased. At low OH exposure, C$_5$H$_{7-11}$O$_{3-8}$NO$_3$ and C$_5$H$_{10}$O$_{2-4}$(NO$_3$)$_2$ signals constituted 24% and 8% of the NO$_3^-$-CIMS signals, respectively (Fig. 2b). The largest signal in this spectrum was m/Q = 259, C$_5$H$_{11}$O$_4$NO$_3$. This compound is likely a second-generation oxidation product that contains two hydroxyl functional groups

and one nitrate functional group (Xiong et al., 2015). A series of additional $C_5H_{9,11}O_{3-8}NO_3$ ions is also detected. The signal observed at m/Q = 288, $C_5H_{10}O_2(NO_3)_2$, is likely a second-generation oxidation product that contains two hydroxyl and two nitrate functional groups (Xiong et al., 2015). Other ion signals potentially associated with dinitrate species included m/Q = 304, $C_5H_{10}O_3(NO_3)_2$, and m/Q = 320, $C_5H_{10}O_4(NO_3)_2$. Related signals were detected at m/Q = 351 and 367, which we assume represent $(HNO_3NO_3^-)C_5H_{10}O_2(NO_3)_2$ and $(HNO_3NO_3^-)C_5H_{10}O_3(NO_3)_2$ because we are not aware of other feasible $(NO_3^-)C_5$ adducts at these mass-to-charge ratios.

At high OH exposure, the same $C_5H_{7-11}O_{3-8}NO_3$ and $C_5H_{10}O_{2-4}(NO_3)_2$ species observed at low OH exposure were detected, but at higher concentrations and at higher dinitrate:nitrate. This is presumably due to higher $NO:HO_2$ achieved at higher I_{254} and fixed $[N_2O]$ (Figs. 1, S1, S4-S5). $C_5H_{7-11}O_{3-8}NO_3$ and $C_5H_{10}O_{2-4}(NO_3)_2$ signals made up 30% and 56%, respectively, of the NO_3^--CIMS spectrum shown in Fig. 2d, where $C_5H_{10}O_2(NO_3)_2$ was the largest signal that is detected.

3.3 NO_3^--CIMS spectra of α-pinene oxidation products

Figure 3 shows NO_3^--CIMS mass spectra of products generated from the oxidation of α-pinene ($C_{10}H_{16}$). Ion signals corresponding to α-pinene oxidation products were colored based on classification in $C_5H_{6-8}O_{5-7}$, $C_{6-9}H_{8-14}O_{6-12}$, $C_{10}H_{14-18}O_{5-14}$, and $C_{19-20}H_{28-32}O_{9-18}$ ion groups containing zero nitrogen atoms; $C_5H_7O_{3-8}NO_3$, $C_{6-9}H_{9-15}O_{5-10}NO_3$, and $C_{10}H_{15-17}O_{4-15}NO_3$ ion groups containing one nitrogen atom; and a $C_{10}H_{16-18}O_{0-7}(NO_3)_2$ ion group containing two nitrogen atoms. As was the case with isoprene oxidation products, we assumed nitrogen atoms present in α-pinene oxidation products were associated with nitrate functional groups formed from RO_2 + NO reactions.

To generate spectra shown in Fig. 3, the reactor was operated at $I_{254} = 2.8 \times 10^{15}$ ph cm^{-2}sec^{-1}, $[H_2O] = 0.07\%$, and $[N_2O]$ = 0 and 3.2%. In this experiment, lower $[H_2O]$ was used to minimize [OH] and facilitate closer comparison with spectra from previous NO_3^--CIMS studies of α-pinene + O_3 oxidation products generated at "low-NO_x" conditions (Ehn et al., 2012, 2014). As shown in Fig. S6, corresponding OH and O_3 exposures ranged from $(0.19 - 1.8) \times 10^{11}$ molec cm^{-3} sec and $(7.2-9.5) \times 10^{16}$ molec cm^{-3} sec for the low- and high-NO_x conditions, respectively.

To first order, at OH and O_3 exposures of 2.1×10^{10} and 7.4×10^{15} molec cm^{-3} sec that are attained at $[N_2O]$ = 3.2%, α-pinene should react once with each oxidant in the gas phase. Thus, at the highest $[N_2O]$ values used, yields of second-generation (or later) α-pinene + OH oxidation products detected with the NO_3^--CIMS were minimized relative to α-pinene + O_3 first-generation oxidation products, as desired (Jokinen et al., 2015). However, a potential consequence of using $O(^1D)$ + N_2O reactions to study the NO_x-dependence of chemical systems similar to those examined by Ehn et al. (2012, 2014) is that RO_2 may be produced from α-pinene + NO_3 reactions in addition to α-pinene + O_3 or α-pinene + OH reactions (Sect. 2.1 and Fig. S6).

3.3.1 NO_3^--CIMS mass spectral features observed at "low NO_x" conditions

Of the signal detected at "low-NO_x" conditions (Fig. 3a), $C_5H_{6-8}O_{5-7}$, $C_{6-9}H_{8-14}O_{6-12}$, $C_{10}H_{14-18}O_{5-14}$, and $C_{19-20}H_{28-32}O_{9-18}$ ion groups comprised 6%, 23%, 54%, and 5%, respectively. The C_{10} monomers and C_{19-20} dimers compounds that were observed are often associated with atmospheric new particle formation events (Ehn et al., 2014). The prominent $C_{10}H_{14,16}O_{7-9}$

ion signals detected at m/Q = 308, 310, 324, 326, 340 and 342 in our measurements were dominant signals in previous laboratory and field experiments influenced by the ozonolysis of α-pinene emissions (Ehn et al., 2010, 2012, 2014; Jokinen et al., 2015). Other ion signals that were observed correspond to C_{5-9} species that were generated following carbon-carbon bond cleavage of the C_{10} carbon backbone (Ehn et al., 2012). The remaining $\sim$13% of the signal was classified into $C_5H_7O_{6-11}NO_3$, $C_{6-9}H_{9-15}O_{5-10}NO_3$, and $C_{10}H_{15-17}O_{4-15}NO_3$ ion groups and may be due to background NO_x in the reactor (Sect. 2.1).

3.3.2 NO_3^--CIMS mass spectral features observed at "high NO_x" conditions

As was the case with NO_3^--CIMS spectra of isoprene oxidation products, the addition of N_2O to the reactor significantly changed the mass spectrum of α-pinene oxidation products (Fig. 3b). At $[N_2O]$ = 3.2%, organic nitrates and dinitrates comprised 65% of the total ion signal (Fig. 3b inset). We observed reduction in $C_{6-9}H_{8-14}O_{6-12}$, $C_{10}H_{14-18}O_{5-14}$, and $C_{19-20}H_{28-32}O_{9-18}$ ion signals, along with increases in $C_5H_{6-8}O_{5-7}$, $C_5H_7O_{3-8}NO_3$, $C_{6-9}H_{9-15}O_{2-7}NO_3$, $C_{10}H_{15-17}O_{1-11}NO_3$ and $C_{10}H_{16-18}O_{0-7}(NO_3)_2$ signals. The C_{10} dinitrates may originate from two α-pinene + OH reactions followed by two RO_2 + NO reactions, but may also include contributions from one α-pinene + NO_3 reaction followed by one RO_2 + NO reaction. The largest ion signal in Fig. 3b was observed at m/Q = 240, $C_5H_6O_7$. The largest organic nitrate signals in this spectrum were at m/Q = 329, $C_8H_{13}O_6NO_3$, followed by $C_{10}H_{15}O_6NO_3$ (m/Q = 355), $C_{10}H_{16}O_3(NO_3)_2$ (m/Q = 354), and $C_{10}H_{15}O_5NO_3$ (m/Q = 339).

3.4 Transition from RO_2+HO_2 to RO_2+NO-dominant regimes observed in isoprene and α-pinene oxidation products

Figures 4 and 5 shows normalized signals of the representative groups of isoprene and α-pinene oxidation products as a function of increasing $NO:HO_2$. For each group of compounds, signals obtained at a specific $NO:HO_2$ were normalized to the maximum observed signal. $NO:HO_2$ is correlated with the relative branching ratios of RO_2 + HO_2 and RO_2 + NO reactions that govern the distribution of oxidation products observed in Figs. 2 and 3. As is evident from Figs. 4 and 5, different ion families were characterized by different trends as a function of $NO:HO_2$. The normalized signals of C_{4-5} (isoprene), C_{6-10} (α-pinene) and C_{19-20} (α-pinene) species decreased monotonically with increasing $NO:HO_2$. In Fig. 5, the abundance of C_{19-20} dimers decreased significantly faster than the C_{6-10} species. Because dimers are products of RO_2 + RO_2 self-reactions, their yield is quadratic with respect to $[RO_2]$ and therefore was more affected by competing RO_2 + NO reactions than species formed from RO_2 + HO_2 reactions.

The normalized signals of C_5 (isoprene) and C_{10} (α-pinene) organic nitrates reached their maximum values at $NO:HO_2 \approx$ 1 prior to decreasing. Maximum signals of C_{6-9} organic nitrates (α-pinene) were obtained at $NO:HO_2$ = 2.4, and maximum signals of C_5 (isoprene) and C_{10} (α-pinene) dinitrates were obtained at $NO:HO_2$ = 5.2 and 6.4. The formation of dinitrates was favored when RO_2 + NO $>>$ RO_2 + HO_2, as expected, and regardless of whether RO_2 was formed from oxidation of α-pinene by OH, O_3 or NO_3. We hypothesize that $NO:HO_2 >> 1$ favored RO_2 + NO fragmentation reactions that led to formation of smaller, more volatile $C_5H_{6-8}O_{5-7}$ and $C_5H_7O_{3-8}NO_3$ α-pinene oxidation products (Atkinson, 2007; Chacon-Madrid and Donahue, 2011), whose signals continuously increased with increasing $NO:HO_2$, along with other products not detected with

NO_3^--CIMS. This pathway apparently competed with NO_x-influenced auto-oxidation processes that led to formation of C_5 isoprene dinitrates, C_6-C_{10} α-pinene nitrates and C_{10} α-pinene dintrates.

Isoprene oxidation products such as $C_5H_9O_4NO_3$ and $C_5H_{11}O_4NO_3$ contain one peroxide and one nitrate functional group, and $C_5H_9O_5NO_3$ contains two peroxide and one nitrate functional group. The formation of these species, as well as C_{6-10} α-pinene-derived organic nitrates, was favored at $NO:HO_2 \approx$ 1-2 where the relative rates of $RO_2 + NO$ and $RO_2 + HO_2$ reactions were similar. This correlation suggests that the C_{6-10} α-pinene organic nitrates detected with NO_3^--CIMS contained a combination of peroxide and nitrate functional groups, whereas C_5 (isoprene) and C_{10} (α-pinene) dinitrates contained fewer functional groups that were specifically formed from $RO_2 + HO_2$ reactions.

4 Atmospheric Implications

The use of $O(^1D) + N_2O$ reactions in oxidation flow reactors facilitates systematic control of $NO:HO_2$ over the range of "$RO_2 + HO_2$ dominant" to "$RO_2 + NO$ dominant" conditions. Further, this is accomplished with the use of a single OH radical precursor (O_3) that has previously hindered characterization of NO_x-dependent chemistry in oxidation flow reactors. Our results suggest that this method can be used to identify molecular tracers for processes influenced by $RO_2 + NO$ and/or $RO_2 + NO_2$ reactions. For example, $C_5H_{7-11}O_{3-8}NO_3$ compounds formed from the oxidation of isoprene were detected in air masses influenced by mixed isoprene and anthropogenic emissions (Lee et al., 2016). Similarly, $C_{10}H_{15}O_{5-8}NO_3$ compounds formed from the oxidation of α-pinene were detected in air masses influenced by α-pinene emissions that were subsequently oxidized by O_3 in the presence of NO (Yan et al., 2016).

This method will be used in future work to investigate the influence of NO_x on physicochemical properties of secondary organic aerosols such as hygroscopicity and refractive indices over an atmospherically relevant range of $NO:HO_2$. Care should be taken to use experimental conditions that minimize the relative contributions of unwanted NO_3-initiated oxidation chemistry, particularly when using species such as α-pinene that are highly reactive to NO_3. While potential formation of dinitrates from α-pinene + NO_3 reactions at high-NO conditions was not the primary goal of this experiment, we note that this chemical fingerprint has been observed in ambient measurements (Yan et al., 2016) and thus represents an additional application of $O(^1D) + N_2O$ reactions in future work. Additionally, studies that require multiple days of equivalent atmospheric OH oxidation at $NO:HO_2 \gg 1$ should consider implementing 185 nm photolysis of H_2O and N_2O to provide additional sources of $O(^1D)$ and OH that may decrease OH suppression due to competing $O(^1D) + H_2O$ and $O(^1D) + N_2O$ reactions.

Acknowledgements. This research was supported by the Atmospheric Chemistry Program of the U.S. National Science Foundation under grants AGS-1536939, AGS-1537446 and AGS-1537009 and by the U.S. Office of Science (BER), Department of Energy (Atmospheric Systems Research) under grants DE-SC0006980 and DE-SC0011935. A. T. Lambe thanks Conner Daube (ARI) for help with supporting measurements as well as Gabriel Isaacman-VanWertz (MIT), Jesse Kroll (MIT), Zhe Peng (UC Boulder), and Jose Jimenez (UC Boulder) for helpful discussions.

References

Andreae, M. O. and Gelencsér, A.: Black carbon or brown carbon? The nature of light-absorbing carbonaceous aerosols, Atmospheric Chemistry and Physics, 6, 3131–3148, 2006.

Atkinson, R.: Kinetics and mechanisms of the gas-phase reactions of the hydroxyl radical with organic compounds under atmospheric conditions, Chemical Reviews, 86, 69–201, 1986.

Atkinson, R.: Kinetics and Mechanisms of the Gas-Phase Reactions of the NO3 Radical with Organic Compounds, Journal of Physical and Chemical Reference Data, 20, 459–507, doi:http://dx.doi.org/10.1063/1.555887, http://scitation.aip.org/content/aip/journal/jpcrd/20/3/10.1063/1.555887, 1991.

Atkinson, R.: Rate constants for the atmospheric reactions of alkoxy radicals: An updated estimation method, Atmospheric Environment, 41, 8468–8485, 2007.

Bertram, T. H., Kimmel, J. R., Crisp, T. A., Ryder, O. S., Yatavelli, R. L. N., Thornton, J. A., Cubison, M. J., Gonin, M., and Worsnop, D. R.: A field-deployable, chemical ionization time-of-flight mass spectrometer, Atmospheric Measurement Techniques, 4, 1471–1479, 2011.

Bruns, E. A., Krapf, M., Orasche, J., Huang, Y., Zimmermann, R., Drinovec, L., Močnik, G., El Haddad, I., Slowik, J. G., Dommen, J., Baltensperger, U., and Prevot, A. S. H.: Characterization of primary and secondary wood combustion products generated under different burner loads, Atmospheric Chemistry and Physics, 15, 2825–2841, 2015.

Carlton, A., Pinder, R., Bhave, P., and Pouliot, G.: To What Extent Can Biogenic SOA be Controlled?, Environmental Science and Technology, 44, 3376–3380, 2010.

Carslaw, K. S., Lee, L. A., Reddington, C. L., Pringle, K. J., Rap, A., Forster, P. M., Mann, G. W., Spracklen, D. V., Woodhouse, M. T., Regayre, L. A., and Pierce, J. R.: Large contribution of natural aerosols to uncertainty in indirect forcing, Nature, 503, 67–71, 2014.

Chacon-Madrid, H. J. and Donahue, N. M.: Fragmentation vs. functionalization: chemical aging and organic aerosol formation, Atmospheric Chemistry and Physics, 11, 10 553–10 563, 2011.

Crounse, J. D., Nielsen, L. B., Jørgensen, S., Kjaergaard, H. G., and Wennberg, P. O.: Autoxidation of Organic Compounds in the Atmosphere, The Journal of Physical Chemistry Letters, 4, 3513–3520, 2013.

Donahue, N. M., Kroll, J. H., Pandis, S. N., and Robinson, A. L.: A two-dimensional volatility basis set – Part 2: Diagnostics of organic-aerosol evolution, Atmospheric Chemistry and Physics, 12, 615–634, 2012.

Donahue, N. M., Ortega, I. K., Chuang, W., Riipinen, I., Riccobono, F., Schobesberger, S., Dommen, J., Baltensperger, U., Kulmala, M., Worsnop, D. R., and Vehkamäki, H.: How do organic vapors contribute to new-particle formation?, Faraday Discussions, 165, 91, 2013.

Ehn, M., Junninen, H., Petäjä, T., Kurtén, T., Kerminen, V.-M., Schobesberger, S., Manninen, H. E., Ortega, I. K., Vehkamäki, H., Kulmala, M., and Worsnop, D. R.: Composition and temporal behavior of ambient ions in the boreal forest, Atmospheric Chemistry and Physics, 10, 8513–8530, 2010.

Ehn, M., Kleist, E., Junninen, H., Petäjä, T., Lönn, G., Schobesberger, S., Dal Maso, M., Trimborn, A., Kulmala, M., Worsnop, D. R., Wahner, A., Wildt, J., and Mentel, T. F.: Gas phase formation of extremely oxidized pinene reaction products in chamber and ambient air, Atmospheric Chemistry and Physics, 12, 5113–5127, 2012.

Ehn, M., Thornton, J. A., Kleist, E., Sipilä, M., Junninen, H., Pullinen, I., Springer, M., Rubach, F., Tillmann, R., Lee, B., Lopez-Hilfiker, F., Andres, S., Acir, I.-H., Rissanen, M., Jokinen, T., Schobesberger, S., Kangasluoma, J., Kontkanen, J., Nieminen, T., Kurten, T., Nielsen, L. B., Jørgensen, S., Kjaergaard, H. G., Canagaratna, M., Maso, M. D., Berndt, T., Petäjä, T., Wahner, A., Kerminen, V.-M., Kulmala, M., Worsnop, D. R., Wildt, J., and Mentel, T. F.: A large source of low-volatility secondary organic aerosol, Nature, 506, 476–479, 2014.

Eisele, F. L. and Tanner, D. J.: Measurement of the gas phase concentration of H2SO4 and methane sulfonic acid and estimates of H2SO4 production and loss in the atmosphere, Journal of Geophysical Research: Atmospheres, 98, 9001–9010, doi:10.1029/93JD00031, http://dx.doi.org/10.1029/93JD00031, 1993.

Jokinen, T., Berndt, T., Makkonen, R., Kerminen, V.-M., Junninen, H., Paasonen, P., Stratmann, F., Herrmann, H., Guenther, A. B., Worsnop, D. R., Kulmala, M., Ehn, M., and Sipilä, M.: Production of extremely low volatile organic compounds from biogenic emissions: Measured yields and atmospheric implications, Proceedings of the National Academy of Sciences, 112, 7123–7128, 2015.

Kang, E., Root, M. J., Toohey, D. W., and Brune, W. H.: Introducing the concept of potential aerosol mass (PAM), Atmospheric Chemistry and Physics, 7, 5727–5744, 2007.

Krechmer, J. E., Coggon, M. M., Massoli, P., Nguyen, T. B., Crounse, J. D., Hu, W., Day, D. A., Tyndall, G. S., Henze, D. K., Rivera-Rios, J. C., Nowak, J. B., Kimmel, J. R., Mauldin, III, R. L., Stark, H., Jayne, J. T., Sipilä, M., Junninen, H., Clair, J. M. S., Zhang, X., Feiner, P. A., Zhang, L., Miller, D. O., Brune, W. H., Keutsch, F. N., Wennberg, P. O., Seinfeld, J. H., Worsnop, D. R., Jimenez, J. L., and Canagaratna, M. R.: Formation of Low Volatility Organic Compounds and Secondary Organic Aerosol from Isoprene Hydroxyhydroperoxide Low-NO Oxidation, Environmental Science and Technology, 49, 10 330–10 339, 2015.

Kurtén, T., Petäjä, T., Smith, J., Ortega, I. K., Sipilä, M., Junninen, H., Ehn, M., Vehkamäki, H., Mauldin, L., Worsnop, D. R., and Kulmala, M.: The effect of H_2SO_4 & amine clustering on chemical ionization mass spectrometry (CIMS) measurements of gas-phase sulfuric acid, Atmospheric Chemistry and Physics, 11, 3007–3019, doi:10.5194/acp-11-3007-2011, http://www.atmos-chem-phys.net/11/3007/2011/, 2011.

Lambe, A. T., Ahern, A. T., Williams, L. R., Slowik, J. G., Wong, J. P. S., Abbatt, J. P. D., Brune, W. H., Ng, N. L., Wright, J. P., Croasdale, D. R., Worsnop, D. R., Davidovits, P., and Onasch, T. B.: Characterization of aerosol photooxidation flow reactors: heterogeneous oxidation, secondary organic aerosol formation and cloud condensation nuclei activity measurements, Atmospheric Measurement Techniques, 4, 445–461, 2011a.

Lambe, A. T., Onasch, T. B., Massoli, P., Croasdale, D. R., Wright, J. P., Ahern, A. T., Williams, L. R., Worsnop, D. R., Brune, W. H., and Davidovits, P.: Laboratory studies of the chemical composition and cloud condensation nuclei (CCN) activity of secondary organic aerosol (SOA) and oxidized primary organic aerosol (OPOA), Atmospheric Chemistry and Physics Discussions, 11, 13 617–13 653, 2011b.

Lambe, A. T., Chhabra, P. S., Onasch, T. B., Brune, W. H., Hunter, J. F., Kroll, J. H., Cummings, M. J., Brogan, J. F., Parmar, Y., Worsnop, D. R., Kolb, C. E., and Davidovits, P.: Effect of oxidant concentration, exposure time, and seed particles on secondary organic aerosol chemical composition and yield, Atmospheric Chemistry and Physics, 15, 3063–3075, 2015.

Lee, B. H., Mohr, C., Lopez-Hilfiker, F. D., Lutz, A., Hallquist, M., Lee, L., Romer, P., Cohen, R. C., Iyer, S., Kurten, T., Hu, W., Day, D. A., Campuzano-Jost, P., Jimenez, J. L., Xu, L., Ng, N. L., Guo, H., Weber, R. J., Wild, R. J., Brown, S. S., Koss, A., De Gouw, J., Olson, K., Goldstein, A. H., Seco, R., Kim, S., McAvey, K., Shepson, P. B., Starn, T., Baumann, K., Edgerton, E. S., Liu, J., Shilling, J. E., Miller, D. O., Brune, W., Schobesberger, S., D'Ambro, E. L., and Thornton, J. A.: Highly functionalized organic nitrates in the southeast United States: Contribution to secondary organic aerosol and reactive nitrogen budgets, Proceedings of the National Academy of Sciences, 113, 1516–1521, 2016.

Li, R., Palm, B. B., Ortega, A. M., Hlywiak, J., Hu, W., Peng, Z., Day, D. A., Knote, C., Brune, W. H., De Gouw, J. A., and Jimenez, J. L.: Modeling the Radical Chemistry in an Oxidation Flow Reactor: Radical Formation and Recycling, Sensitivities, and the OH Exposure Estimation Equation, The Journal of Physical Chemistry A, 119, 150406123535 006, 2015.

Liu, J., D'Ambro, E. L., Lee, B. H., Lopez-Hilfiker, F. D., Zaveri, R. A., Rivera-Rios, J. C., Keutsch, F. N., Iyer, S., Kurten, T., Zhang, Z., Gold, A., Surratt, J. D., Shilling, J. E., and Thornton, J. A.: Efficient Isoprene Secondary Organic Aerosol Formation from a Non-IEPOX

Pathway, Environmental Science & Technology, 50, 9872–9880, doi:10.1021/acs.est.6b01872, http://dx.doi.org/10.1021/acs.est.6b01872, pMID: 27548285, 2016.

Liu, P. F., Abdelmalki, N., Hung, H.-M., Wang, Y., Brune, W. H., and Martin, S. T.: Ultraviolet and visible complex refractive indices of secondary organic material produced by photooxidation of the aromatic compounds toluene and *m*-xylene, Atmospheric Chemistry and Physics, 15, 1435–1446, 2015.

Mao, J., Ren, X., Brune, W., Olson, J., Crawford, J., Fried, A., Huey, L., Cohen, R., Heikes, B., and Singh, H.: Airborne measurement of OH reactivity during INTEX-B, Atmospheric Chemistry and Physics, 9, 163–173, 2009.

Merikanto, J., Spracklen, D. V., Mann, G. W., Pickering, S. J., and Carslaw, K. S.: Impact of nucleation on global CCN, Atmospheric Chemistry and Physics, 9, 8601–8616, 2009.

Ng, N. L., Chhabra, P. S., Chan, A., Surratt, J. D., Kroll, J. H., Kwan, A. J., McCabe, D. C., Wennberg, P. O., Sorooshian, A., and Murphy, S. M.: Effect of NOx level on secondary organic aerosol (SOA) formation from the photooxidation of terpenes, Atmospheric Chemistry and Physics, 7, 5159–5174, 2007.

Ng, N. L., Canagaratna, M. R., Zhang, Q., Jimenez, J. L., Tian, J., Ulbrich, I. M., Kroll, J. H., Docherty, K. S., Chhabra, P. S., Bahreini, R., Murphy, S. M., Seinfeld, J. H., Hildebrandt, L., Donahue, N. M., Decarlo, P. F., Lanz, V. A., Prévôt, A. S. H., Dinar, E., Rudich, Y., and Worsnop, D. R.: Organic aerosol components observed in Northern Hemispheric datasets from Aerosol Mass Spectrometry, Atmospheric Chemistry and Physics, 10, 4625–4641, 2010.

Ortega, A. M., Hayes, P. L., Peng, Z., Palm, B. B., Hu, W., Day, D. A., Li, R., Cubison, M. J., Brune, W. H., Graus, M., Warneke, C., Gilman, J. B., Kuster, W. C., De Gouw, J., Gutiérrez-Montes, C., and Jimenez, J. L.: Real-time measurements of secondary organic aerosol formation and aging from ambient air in an oxidation flow reactor in the Los Angeles area, Atmospheric Chemistry and Physics, 16, 7411–7433, 2016.

Palm, B. B., Campuzano-Jost, P., Ortega, A. M., Day, D. A., Kaser, L., Jud, W., Karl, T., Hansel, A., Hunter, J. F., Cross, E. S., Kroll, J. H., Peng, Z., Brune, W. H., and Jimenez, J. L.: In situ secondary organic aerosol formation from ambient pine forest air using an oxidation flow reactor, Atmospheric Chemistry and Physics, 16, 2943–2970, 2016.

Peeters, J., Müller, J.-F., Stavrakou, T., and Nguyen, V. S.: Hydroxyl Radical Recycling in Isoprene Oxidation Driven by Hydrogen Bonding and Hydrogen Tunneling: The Upgraded LIM1 Mechanism, The Journal of Physical Chemistry A, 118, 8625–8643, 2014.

Peng, Z., Day, D. A., Stark, H., Li, R., Lee-Taylor, J., Palm, B. B., Brune, W. H., and Jimenez, J. L.: HO_x radical chemistry in oxidation flow reactors with low-pressure mercury lamps systematically examined by modeling, Atmospheric Measurement Techniques, 8, 4863–4890, 2015.

Peng, Z., Day, D. A., Ortega, A. M., Palm, B. B., Hu, W., Stark, H., Li, R., Tsigaridis, K., Brune, W. H., and Jimenez, J. L.: Non-OH chemistry in oxidation flow reactors for the study of atmospheric chemistry systematically examined by modeling, Atmospheric Chemistry and Physics, 16, 4283–4305, 2016.

Pfaffenberger, L., Barmet, P., Slowik, J. G., Praplan, A. P., Dommen, J., Prevot, A. S. H., and Baltensperger, U.: The link between organic aerosol mass loading and degree of oxygenation: an α-pinene photooxidation study, Atmospheric Chemistry and Physics, 13, 6493–6506, 2013.

Pierce, J. R., Leaitch, W. R., Liggio, J., Westervelt, D. M., Wainwright, C. D., Abbatt, J. P. D., Ahlm, L., Al-Basheer, W., Cziczo, D. J., Hayden, K. L., Lee, A. K. Y., Li, S.-M., Russell, L. M., Sjostedt, S. J., Strawbridge, K. B., Travis, M., Vlasenko, A., Wentzell, J. J. B., Wiebe, H. A., Wong, J. P. S., and Macdonald, A. M.: Nucleation and condensational growth to CCN sizes during a sustained pristine biogenic SOA event in a forested mountain valley, Atmospheric Chemistry and Physics, 12, 3147–3163, 2012.

Pugh, T. A. M., MacKenzie, A. R., Langford, B., Nemitz, E., Misztal, P. K., and Hewitt, C. N.: The influence of small-scale variations in isoprene concentrations on atmospheric chemistry over a tropical rainforest, Atmospheric Chemistry and Physics, 11, 4121–4134, 2011.

Riccobono, F., Schobesberger, S., Scott, C. E., Dommen, J., Ortega, I. K., Rondo, L., Almeida, J., Amorim, A., Bianchi, F., Breitenlechner, M., David, A., Downard, A., Dunne, E. M., Duplissy, J., Ehrhart, S., Flagan, R. C., Franchin, A., Hansel, A., Junninen, H., Kajos, M., Keskinen, H., Kupc, A., Kürten, A., Kvashin, A. N., Laaksonen, A., Lehtipalo, K., Makhmutov, V., Mathot, S., Nieminen, T., Onnela, A., Petäjä, T., Praplan, A. P., Santos, F. D., Schallhart, S., Seinfeld, J. H., Sipilä, M., Spracklen, D. V., Stozhkov, Y., Stratmann, F., Tomé, A., Tsagkogeorgas, G., Vaattovaara, P., Viisanen, Y., Vrtala, A., Wagner, P. E., Weingartner, E., Wex, H., Wimmer, D., Carslaw, K. S., Curtius, J., Donahue, N. M., Kirkby, J., Kulmala, M., Worsnop, D. R., and Baltensperger, U.: Oxidation Products of Biogenic Emissions Contribute to Nucleation of Atmospheric Particles, Science, 344, 717–721, 2014.

Riipinen, I., Yli-Juuti, T., Pierce, J. R., Petäjä, T., Worsnop, D. R., Kulmala, M., and Donahue, N. M.: The contribution of organics to atmospheric nanoparticle growth, Nature Publishing Group, 5, 453–458, 2012.

Rissanen, M. P., Kurten, T., Sipilä, M., Thornton, J. A., Kangasluoma, J., Sarnela, N., Junninen, H., Jørgensen, S., Schallhart, S., Kajos, M. K., Taipale, R., Springer, M., Mentel, T. F., Ruuskanen, T., Petäjä, T., Worsnop, D. R., Kjaergaard, H. G., and Ehn, M.: The Formation of Highly Oxidized Multifunctional Products in the Ozonolysis of Cyclohexene, J. Am. Chem. Soc, 136, 15 596–15 606, 2014.

Sander, S., Friedl, R., DeMore, W., Golden, D., Kurylo, M., Hampson, R. F., Huie, R., Moortgat, G., Ravishankara, A., Kolb, C., and Molina, M. J.: Chemical Kinetics and Photochemical Data for Use in Stratospheric Modeling, Evaluation Number 13, JPL Publication, pp. 1–74, 2000.

Sander, S., Friedl, R., Golden, D., Kurylo, M., Moortgat, G., Keller-Rudek, H., Wine, P., Ravishankara, A. R., Kolb, C., Molina, M., Finlayson-Pitts, B., Huie, R., and Orkin, V.: Chemical Kinetics and Photochemical Data for Use in Atmospheric Studies, Evaluation Number 15, JPL Publication, pp. 1–523, 2006.

Shilling, J., Chen, Q., King, S., Rosenoern, T., Kroll, J., Worsnop, D., Decarlo, P., Aiken, A., Sueper, D., and Jimenez, J.: Loading-dependent elemental composition of alpha-pinene SOA particles, Atmospheric Chemistry and Physics, 9, 771–782, 2009.

Shilling, J. E., Zaveri, R. A., Fast, J. D., Kleinman, L., Alexander, M. L., Canagaratna, M. R., Fortner, E., Hubbe, J. M., Jayne, J. T., Sedlacek, A., Setyan, A., Springston, S., Worsnop, D. R., and Zhang, Q.: Enhanced SOA formation from mixed anthropogenic and biogenic emissions during the CARES campaign, Atmospheric Chemistry and Physics, 13, 2091–2113, 2013.

Spracklen, D. V., Jimenez, J. L., Carslaw, K. S., Worsnop, D. R., Evans, M. J., Mann, G. W., Zhang, Q., Canagaratna, M. R., Allan, J., Coe, H., Mcfiggans, G., Rap, A., and Forster, P.: Aerosol mass spectrometer constraint on the global secondary organic aerosol budget, Atmospheric Chemistry and Physics, 11, 12 109–12 136, 2011.

St Clair, J. M., Rivera-Rios, J. C., Crounse, J. D., Knap, H. C., Bates, K. H., Teng, A. P., Jørgensen, S., Kjaergaard, H. G., Keutsch, F. N., and Wennberg, P. O.: Kinetics and Products of the Reaction of the First-Generation Isoprene Hydroxy Hydroperoxide (ISOPOOH) with OH, The Journal of Physical Chemistry A, 120, 1441–1451, 2016.

Surratt, J., Murphy, S., Kroll, J., Ng, N., Hildebrandt, L., Sorooshian, A., Szmigielski, R., Vermeylen, R., Maenhaut, W., and Claeys, M.: Chemical composition of secondary organic aerosol formed from the photooxidation of isoprene, The Journal of Physical Chemistry A, 110, 9665–9690, 2006.

Tkacik, D. S., Lambe, A. T., Jathar, S., Li, X., Presto, A. A., Zhao, Y., Blake, D., Meinardi, S., Jayne, J. T., Croteau, P. L., and Robinson, A. L.: Secondary Organic Aerosol Formation from in-Use Motor Vehicle Emissions Using a Potential Aerosol Mass Reactor, Environmental Science and Technology, 48, 11 235–11 242, 2014.

Xiong, F., McAvey, K. M., Pratt, K. A., Groff, C. J., Hostetler, M. A., Lipton, M. A., Starn, T. K., Seeley, J. V., Bertman, S. B., Teng, A. P., Crounse, J. D., Nguyen, T. B., Wennberg, P. O., Misztal, P. K., Goldstein, A. H., Guenther, A. B., Koss, A. R., Olson, K. F., De Gouw, J. A., Baumann, K., Edgerton, E. S., Feiner, P. A., Zhang, L., Miller, D. O., Brune, W. H., and Shepson, P. B.: Observation of isoprene hydroxynitrates in the southeastern United States and implications for the fate of NO_x, Atmospheric Chemistry and Physics, 15, 11 257–11 272, 2015.

Xu, L., Guo, H., Boyd, C. M., Klein, M., Bougiatioti, A., Cerully, K. M., Hite, J. R., Isaacman-VanWertz, G., Kreisberg, N. M., Knote, C., Olson, K., Koss, A., Goldstein, A. H., Hering, S. V., De Gouw, J., Baumann, K., Lee, S.-H., Nenes, A., Weber, R. J., and Ng, N. L.: Effects of anthropogenic emissions on aerosol formation from isoprene and monoterpenes in the southeastern United States, Proceedings of the National Academy of Sciences, 112, 37–42, 2015.

Yan, C., Nie, W., Äijälä, M., Rissanen, M. P., Canagaratna, M. R., Massoli, P., Junninen, H., Jokinen, T., Sarnela, N., Häme, S. A. K., Schobesberger, S., Canonaco, F., Yao, L., Prévôt, A. S. H., Petäjä, T., Kulmala, M., Sipilä, M., Worsnop, D. R., and Ehn, M.: Source characterization of highly oxidized multifunctional compounds in a boreal forest environment using positive matrix factorization, Atmospheric Chemistry and Physics, 16, 12 715–12 731, 2016.

Yu, F. and Luo, G.: Simulation of particle size distribution with a global aerosol model: contribution of nucleation to aerosol and CCN number concentrations, Atmospheric Chemistry and Physics, 9, 7691–7710, 2009.

Zhang, X., Cappa, C. D., Jathar, S. H., McVay, R. C., Ensberg, J. J., Kleeman, M. J., and Seinfeld, J. H.: Influence of vapor wall loss in laboratory chambers on yields of secondary organic aerosol, Proceedings of the National Academy of Sciences, 111, 5802–5807, 2014.
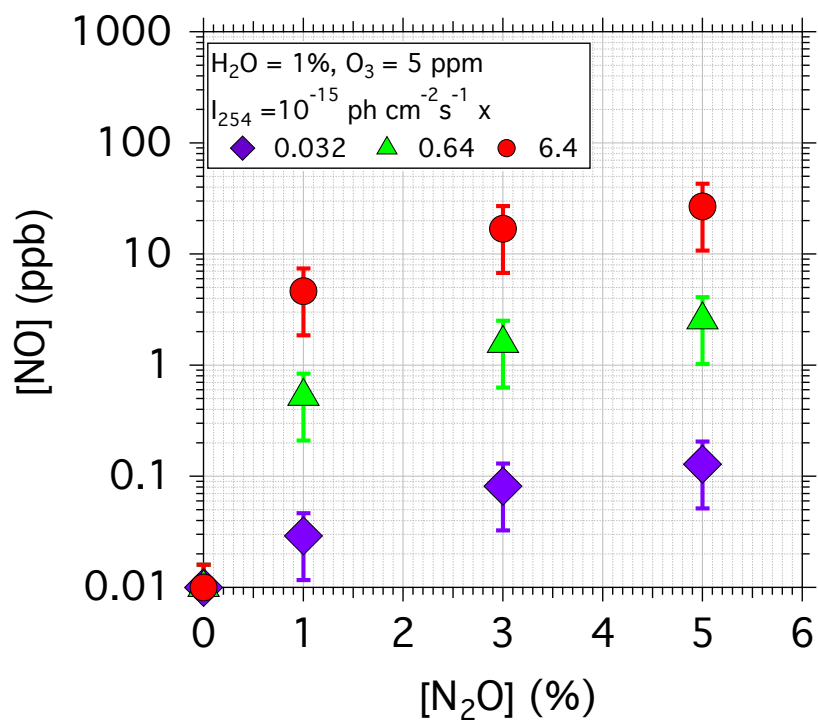
Figure 1. Modeled steady-state [NO] as a function of [N$_2$O] input to the PAM oxidation flow reactor at I$_{254}$ = 0.032×10^{15}, 0.64×10^{15} and 6.4×10^{15} ph cm^{-2} sec, [H$_2$O] = 1%, [O$_3$] = 5 ppm, mean residence time = 80 sec. Error bars represent ± 60% uncertainty in modeled [NO] (Peng et al., 2015).
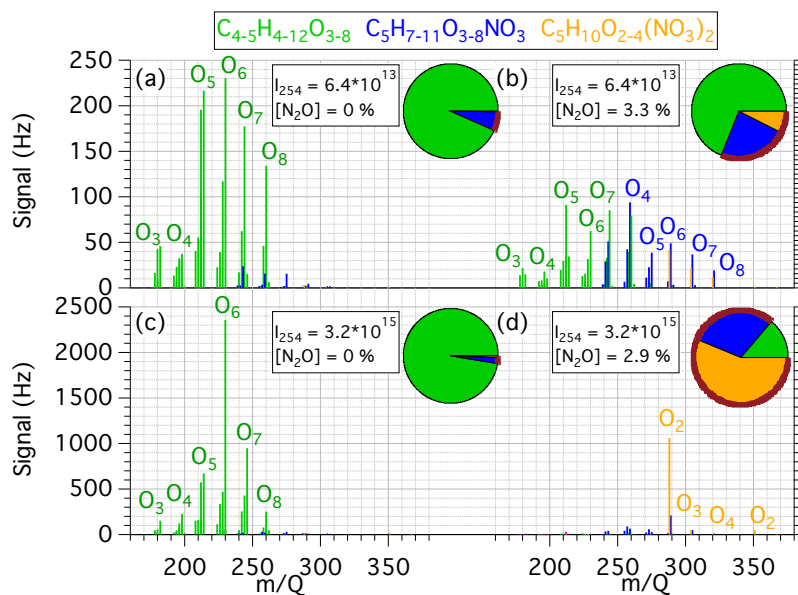
Figure 2. NO_3^--CIMS mass spectra of isoprene oxidation products generated at $[H_2O] = 1\%$, $[O_3] = 5$ ppm, mean residence time = 80 sec: (a) $I_{254} = 6.4 \times 10^{13}$ ph cm^{-2} sec^{-1}, $[N_2O] = 0\%$; (b) $I_{254} = 6.4 \times 10^{13}$ ph cm^{-2} sec^{-1}, $[N_2O] = 3.2$ %; (c) $I_{254} = 3.2 \times 10^{15}$ ph cm^{-2} sec^{-1}, $[N_2O] = 0$ %; (d) $I_{254} = 3.2 \times 10^{15}$ ph cm^{-2} sec^{-1}, $[N_2O] = 2.9$ %. Colors are based on classification in $C_{4-5}H_{4-12}O_{3-8}$, $C_5H_{7-11}O_{3-8}NO_3$, and $C_5H_{10}O_{2-4}(NO_3)_2$ ion groups, with fractional contributions indicated in inset pie charts (brown outline = organonitrate). "O_x" indicate number of oxygen atoms in labeled ions (not including oxygen atoms in nitrate functional groups).
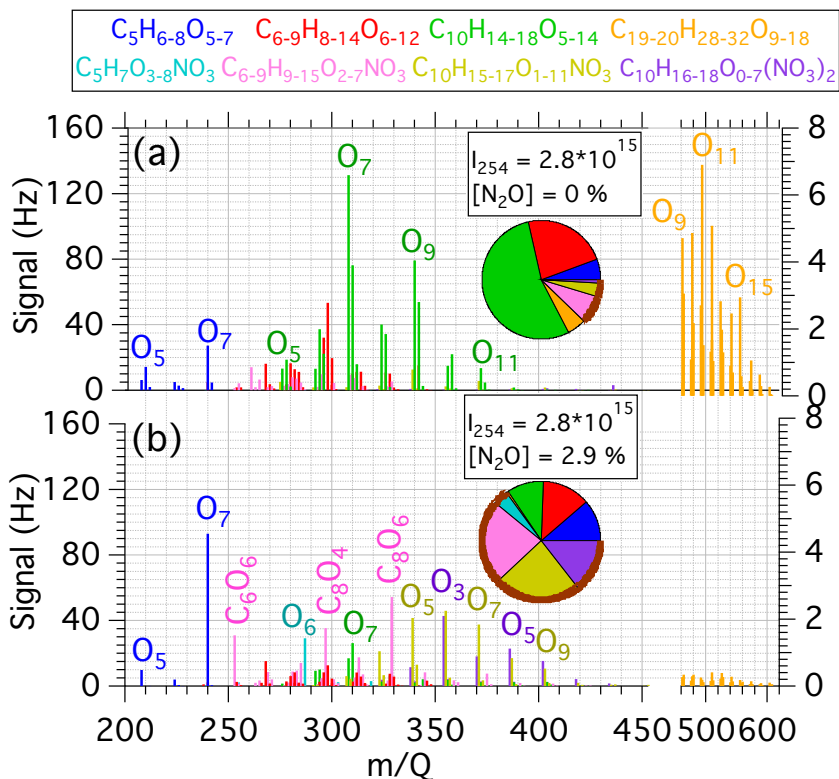
Figure 3. NO_3^--CIMS mass spectra of α-pinene oxidation products generated at $[H_2O] = 0.07\%$, $[O_3] = 5$ ppm, mean residence time = 80 sec: (a) $I_{254} = 2.8 \times 10^{15}$ ph cm^{-2}sec^{-1}, $[N_2O] = 0$ %; (b) $I_{254} = 2.8 \times 10^{15}$ ph cm^{-2}sec^{-1}, $[N_2O] = 3.2$ %. Colors are based on classification in $C_5H_{6-8}O_{5-7}$, $C_{6-9}H_{8-14}O_{6-12}$, $C_{10}H_{14-18}O_{5-14}$, $C_{19-20}H_{28-32}O_{9-18}$, $C_5H_7O_{3-8}NO_3$, $C_{6-9}H_{9-15}O_{2-7}NO_3$, $C_{10}H_{15-17}O_{1-11}NO_3$, and $C_{10}H_{16-18}O_{0-7}(NO_3)_2$ ion groups. Fractional contributions of each species type indicated in inset pie charts (brown outline = organonitrate). "O_x" labels indicate number of oxygen atoms in corresponding signals (not including oxygen atoms in nitrate functional groups).
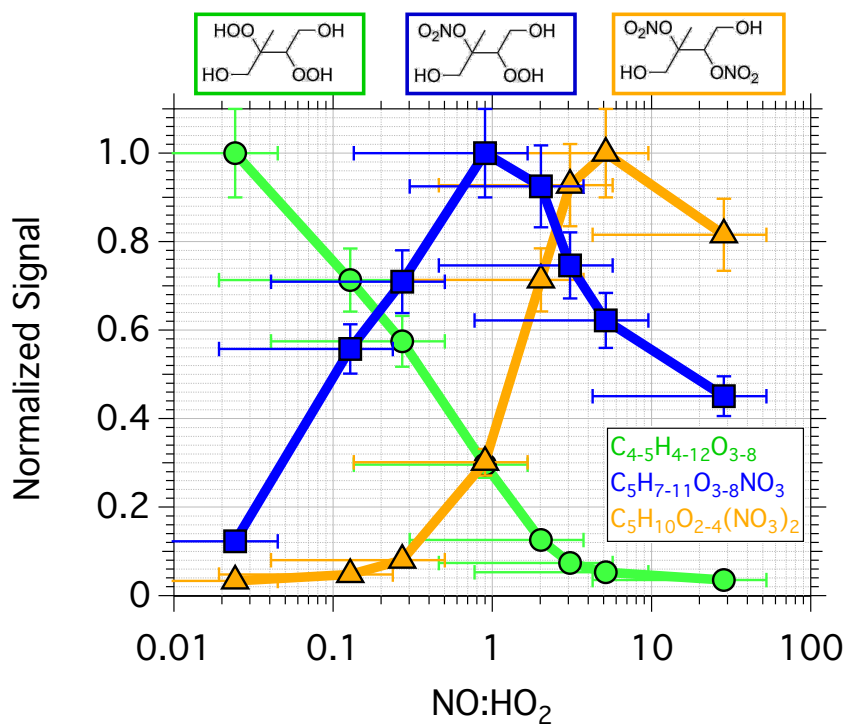
Figure 4. Normalized signals of $C_{4-5}H_{4-12}O_{3-8}$, $C_5H_{7-11}O_{3-8}NO_3$, and $C_5H_{10}O_{2-4}(NO_3)_2$ isoprene oxidation products as a function of modeled $NO:HO_2$. For each of the species classes, signals were normalized to the maximum signal. Representative error bars indicate $\pm$ 1σ uncertainty in NO_3^--CIMS signals and $\pm$ 85% uncertainty in $NO:HO_2$.
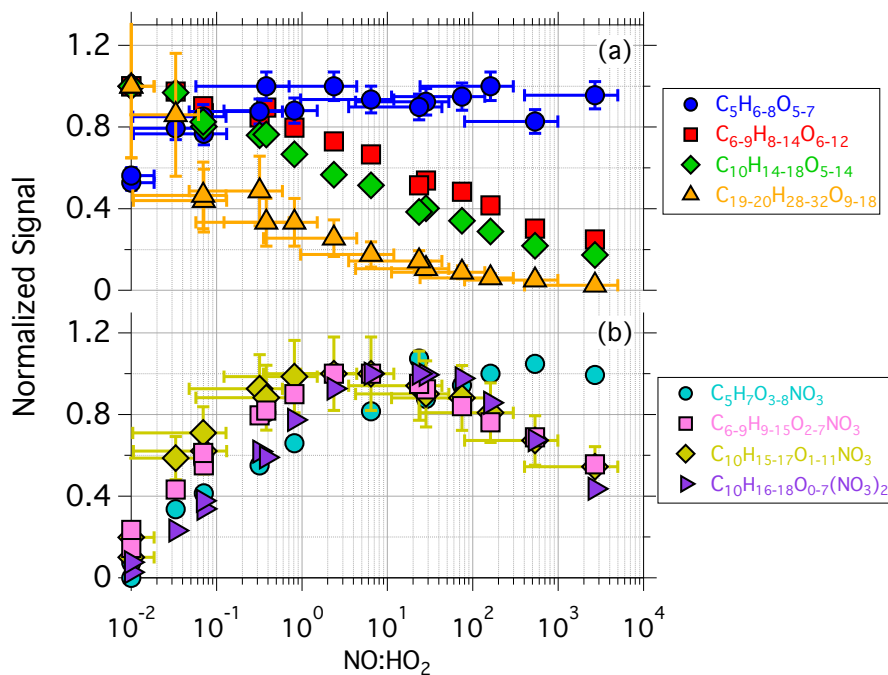
Figure 5. Normalized signals of (a) $C_5H_{6-8}O_{5-7}$, $C_{6-9}H_{8-14}O_{6-12}$, $C_{10}H_{14-18}O_{5-14}$, $C_{19-20}H_{28-32}O_{9-18}$ and (b) $C_5H_7O_{3-8}NO_3$, $C_{6-9}H_{9-15}O_{2-7}NO_3$, $C_{10}H_{15-17}O_{1-11}NO_3$, and $C_{10}H_{16-18}O_{0-7}(NO_3)_2$ α-pinene oxidation products as a function of modeled NO:HO$_2$. For each of the species classes, signals were normalized to the maximum signal. Representative error bars indicate $\pm\,1\sigma$ uncertainty in NO$_3^-$-CIMS signals and $\pm\,85\%$ uncertainty in modeled NO:HO$_2$.